



## Crustal motion in the zone of the 1960 Chile earthquake: Detangling earthquake-cycle deformation and forearc-sliver translation

**Kelin Wang**

*Pacific Geoscience Centre, Geological Survey of Canada, 9860 West Saanich Road, Sidney, British Columbia, Canada  
V8L 4B2 (kwang@nrcan.gc.ca)*

**Yan Hu**

*School of Earth and Ocean Sciences, University of Victoria, Victoria, British Columbia, Canada V8P 5C2  
(yanhu@uvic.ca)*

**Michael Bevis and Eric Kendrick**

*School of Earth Sciences, Ohio State University, 125 South Oval Mall, Columbus, Ohio 43210, USA (mbevis@osu.edu)*

**Robert Smalley Jr.**

*Center for Earthquake Research and Information, University of Memphis, 3890 Central Avenue, Suite 1, Memphis,  
Tennessee 38152, USA (smalley@ceri.memphis.edu)*

**Rodrigo Barriga Vargas**

*Instituto Geográfico Militar, Avenida Santa Isabel 1640, Santiago Centro, Region Metropolitana, Chile*

**Eduardo Lauría**

*Instituto Geográfico Militar de Argentina, Cabildo 381, 1426 Buenos Aires, Argentina*

[1] Temporary deformation in great earthquake cycles and permanent shear deformation associated with oblique plate convergence both provide critical clues for understanding geodynamics and earthquake hazard at subduction zones. In the region affected by the  $M_w$  9.5 great Chile earthquake of 1960, we have obtained GPS observations that provide information on both types of deformation. Our velocity solutions for the first time span the entire latitudinal range of the 1960 earthquake. The new observations revealed a pattern of opposing (roughly arc-normal) motion of coastal and inland sites, consistent with what was reported earlier for the northern part of this region. This finding supports the model of prolonged postseismic deformation as a result of viscoelastic stress relaxation in the mantle. The new observations also provide the first geodetic evidence for the dextral motion of an intravolcanic arc fault system and the consequent northward translation of a forearc sliver. The sliver motion can be modeled using a rate of 6.5 mm/a, accommodating about 30% of the margin-parallel component of Nazca–South America relative plate motion, with the rate diminishing to the north. Furthermore, the new GPS observations show a southward decrease in margin-normal velocities of the coastal area. We prefer explaining the southward decrease in terms of changes in the width or frictional properties of the megathrust seismic zone. Because of the much younger age of the subducting plate and warmer thermal regime in the south, the currently locked portion of the plate interface may be narrower. Using a three-dimensional viscoelastic finite element model of postseismic and interseismic deformation following the 1960 earthquake, we demonstrate that this explanation, although not unique, is consistent with the GPS observations to the first order.

**Components:** 8464 words, 5 figures, 2 tables.

**Keywords:** 1960 Chile earthquake; GPS; interseismic deformation; forearc deformation; viscoelastic stress relaxation; finite element modeling.

**Index Terms:** 1242 Geodesy and Gravity: Seismic cycle related deformations (6924, 7209, 7223, 7230); 8170 Tectonophysics: Subduction zone processes (1031, 3060, 3613, 8413); 9360 Geographic Location: South America.

**Received** 12 June 2007; **Revised** 25 July 2007; **Accepted** 7 August 2007; **Published** 18 October 2007.

Wang, K., Y. Hu, M. Bevis, E. Kendrick, R. Smalley Jr., R. B. Vargas, and E. Lauría (2007), Crustal motion in the zone of the 1960 Chile earthquake: Detangling earthquake-cycle deformation and forearc-sliver translation, *Geochem. Geophys. Geosyst.*, 8, Q10010, doi:10.1029/2007GC001721.

## 1. Introduction

[2] The world's largest recorded earthquake, with a moment magnitude  $M_w = 9.5$ , occurred in 1960 at the Chile margin where the Nazca plate is subducting beneath the South America plate at a rate of about 66 mm/a (Figure 1). Kendrick *et al.* [1997] first reported anomalous coastward motion of a continuous Global Positioning System (GPS) site landward of the rupture zone of the earthquake, and Klotz *et al.* [2001] reported that sites of a GPS network, measured in 1994 and 1996, showed a pattern of opposing motion of coastal and inland sites in the region affected by this earthquake. While all coastal sites move landward, consistent with the current locking of the subduction megathrust, a group of inland sites move seaward (Figure 1, green arrows). Khazaradze *et al.* [2002] and Hu *et al.* [2004] explained the seaward motion as the result of prolonged postseismic deformation due to viscoelastic stress relaxation following the 1960 earthquake. However, these previous studies were limited by the spatial distribution of the then available GPS measurements. The data covered only the northern half of the 1960 rupture region (north of  $\sim 42^\circ\text{S}$ ), although they also spanned a vast region further north.

[3] Project CAP began observing this region in 1993, and although its GPS network has been occupied on a piecemeal basis, by the end of year 2005 nearly all stations had been occupied at least twice and most had been occupied three times. The along-strike coverage of our measurements overlaps the southernmost part of that of Klotz *et al.* [2001] but extends farther south and beyond the southern terminus of the 1960 rupture (Figure 1, red arrows). Our measurements not only have confirmed the opposing motion of coastal and inland sites reported by Klotz *et al.* [2001] north

of  $42^\circ\text{S}$ , but also have shown that the seaward motion of inland sites persists south of  $42^\circ\text{S}$  and throughout the 1960 rupture region. In addition, the new data have revealed two new features of crustal motion in the southern area (Figure 1). First, near-coast GPS velocities in the southern part of the 1960 rupture region have a much smaller landward component than do those further north. Second, although the landward motion becomes smaller as we move south along the coast, the margin-parallel motion does not decrease, indicating a northward "rigid-body" translation.

[4] The expanded GPS data coverage provides an opportunity for further testing the concept of prolonged postseismic deformation and to explore other processes that contribute to crustal deformation at subduction zones. The purpose of this paper is threefold: (1) to present the new GPS data, (2) to demonstrate that the above mentioned margin-parallel motion of the coastal area is consistent with the northward translation of a forearc sliver as previously inferred from geological evidence, and (3) to refine the post-1960 viscoelastic deformation model of Hu *et al.* [2004] in the light of the new observations, especially the much smaller landward velocities of the coastal area in the south.

## 2. GPS Observations

[5] Unlike most GPS projects, our network in the zone of the 1960 rupture was not repeatedly occupied during a small number of large GPS campaigns. Instead, after initial and large campaigns in 1993 (north of  $\sim 42.5^\circ\text{S}$ ) and in 1994 (south of  $\sim 42.5^\circ\text{S}$ ) which barely overlapped, the network south of about  $42^\circ\text{S}$  was occupied on a piecemeal basis, often using just one or two roving GPS receivers, over extended periods of time between 1997 and 2005. We present horizontal

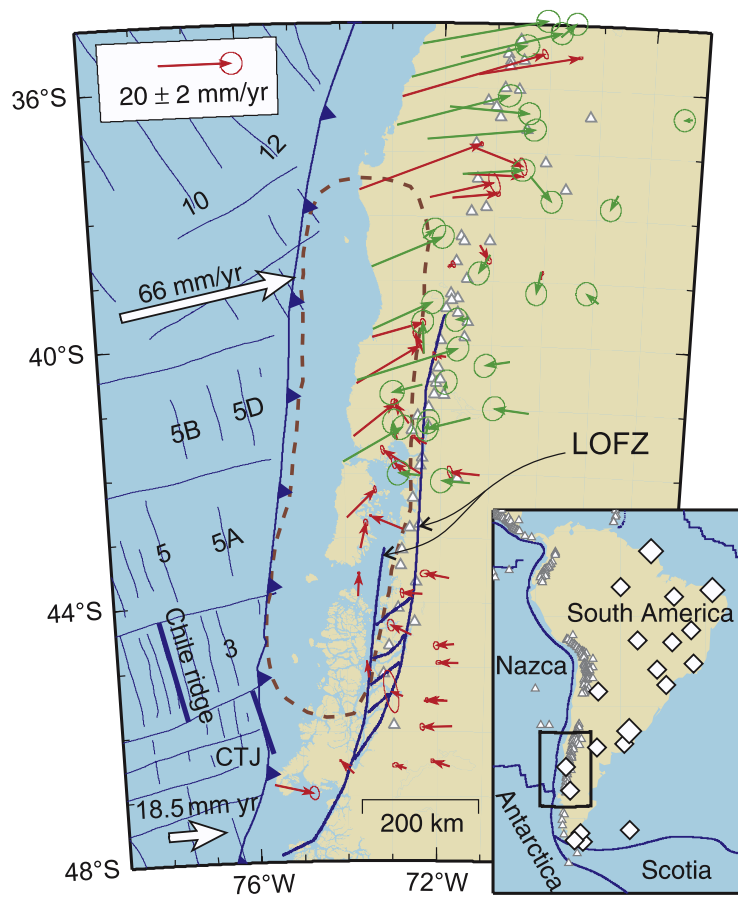


**Figure 1.** Tectonic setting of the Chile margin and GPS velocities. Labeled large arrows are plate motion vectors relative to South America. Triangles indicate locations of volcanoes. New GPS velocities reported in this paper (Table 1) are shown with red arrows. GPS velocities published by Klotz *et al.* [2001] are shown with green arrows. The error ellipse represents one standard deviation. The dashed line approximately indicates the rupture zone of the  $M_w$  9.5 1960 earthquake [Plafker, 1972]. LOFZ, Liqueine-Ofqui Fault Zone [Cembrano *et al.*, 2002]; CTJ, Chile triple junction. Offshore NW- and NE-trending lines represent magnetic lineations and transform faults, respectively. The index numbers of the seafloor magnetic anomalies are as shown by Cifuentes [1989]. Inset shows the large-scale tectonic environment, with GPS stations used to define the South America reference (Table 2) indicated using open diamonds, including the three stations used by Klotz *et al.* [2001] shown as larger diamonds.

velocity solutions for all our stations with a total observational time span of 4.5 a or greater (Table 1). These data were analyzed using the GAMIT and GLOBK software, following procedures previously described by Kendrick *et al.* [2001, 2003] and Brooks *et al.* [2003]. We impose a “cratonic” reference frame which “fixes” the stable core of the South America plate. This frame was realized by minimizing the horizontal velocities of 15 stations located in stable parts of the plate (including Ascension Island), and minimizing the vertical velocities of 33 stations located in the South America and several adjacent plates (Table 2). The root-mean-square horizontal velocity of the 15 “horizontal control” stations used to impose the reference frame was 0.6 mm/a.

[6] These solutions are combined with the previously published solutions of our sister project SAGA led by GeoForschungsZentrum, Potsdam, in Germany [Klotz *et al.*, 2001] in Figure 1. In this latitude range, at least, the horizontal velocity bias between our frame and that used by SAGA is small ( $\sim 1$  mm/a) and can be neglected.

### 3. Liqueine-Ofqui Fault Zone (LOFZ) and Forearc Sliver Motion

[7] The Liqueine-Ofqui Fault Zone (LOFZ) is a fault system of up to 100 km width co-located with the southern Andean volcanic arc (Figures 1 and 2). Its right-lateral shear motion accommodates a significant part of the strike-parallel component

**Table 1.** GPS Site Velocity<sup>a</sup>

Station	Longitude	Latitude	Ve	Vn	Vu	sigVe	sigVn	sigVu	CorNE	Tspan
ALLN	-72.19572	-40.77213	14.45	25.94	-1.67	0.39	0.85	0.85	-0.3906	4.814
ANTC	-71.53205	-37.33870	15.02	-0.42	-1.65	0.06	0.11	0.11	-0.3399	8.832
BLMC	-71.69264	-45.91463	-8.03	-0.36	5.18	0.41	0.62	0.62	-0.2010	8.490
BMNS	-73.73379	-40.58712	17.22	10.13	-1.65	0.34	0.39	0.42	-0.2010	6.713
BSON	-71.20485	-42.01391	-7.93	0.63	0.29	0.51	1.09	1.10	-0.4698	10.263
CARA	-75.63689	-46.80321	10.61	-2.49	4.14	0.85	1.21	1.22	-0.1036	5.740
CBCO	-72.78942	-45.45037	-3.06	1.16	7.84	1.38	3.85	3.86	-0.5193	5.164
CBQA	-72.80183	-36.13834	39.01	11.76	-3.15	0.52	0.85	1.05	-0.5744	4.071
CCVC	-71.90599	-38.78674	1.47	0.80	3.64	0.36	0.58	0.65	-0.4825	10.783
CHCH	-71.73384	-46.53889	-4.59	1.43	5.15	0.33	0.37	0.37	-0.1084	9.836
CHIO	-71.93179	-40.18609	-2.98	0.27	1.85	0.35	0.77	0.83	-0.6902	4.795
CHT2	-72.79946	-42.85511	-8.64	3.45	9.08	0.18	0.19	0.19	0.0194	4.832
CORR	-68.35458	-36.15396	4.58	-0.17	1.92	0.53	0.48	0.52	-0.0387	10.266
COYQ	-71.89208	-45.51434	-4.98	-0.20	-0.07	0.09	0.13	0.13	-0.1376	7.485
DLGN	-71.81453	-45.52049	-5.37	0.07	1.58	0.24	0.43	0.43	-0.3413	10.019
ESTQ	-73.79999	-41.41064	11.45	9.04	3.53	0.23	0.40	0.39	-0.2009	10.816
FECPH	-72.67475	-41.21869	-3.89	5.43	9.37	0.69	0.78	0.76	-0.0146	10.814
FTRN	-72.37671	-40.13039	-2.44	5.18	6.76	0.31	0.71	0.73	-0.5181	10.805
HNCO	-73.96592	-42.67819	7.76	7.64	5.91	0.23	0.63	0.60	-0.2532	5.768
LCPG	-71.82284	-37.70998	12.38	1.25	-0.62	0.39	0.38	0.38	0.0116	10.767
LEBU	-73.64339	-37.57926	33.60	12.38	-16.20	0.27	0.32	0.35	-0.1866	10.786
LHCL	-65.59525	-38.00266	-0.31	-0.62	-1.17	0.08	0.11	0.11	-0.2161	8.400
LO10	-68.47272	-46.04242	-11.75	5.27	-25.61	0.98	0.73	0.72	0.0995	4.972
LQMY	-71.27235	-38.44978	2.40	-3.97	-3.17	0.50	0.64	0.70	-0.2801	4.567
LSRF	-73.87044	-46.64516	-3.60	3.44	8.09	0.14	0.18	0.18	-0.0769	10.011
MCHN	-72.25869	-37.69691	17.42	4.13	0.99	1.06	1.97	2.19	-0.5277	4.655
MFNT	-71.58023	-44.93283	-5.31	-0.03	-0.28	0.50	0.34	0.34	0.1152	4.961
MLKA	-73.74928	-43.89679	0.29	6.22	16.86	0.22	0.18	0.17	0.1677	10.538
MONA	-72.60508	-44.50118	-5.52	2.54	-0.05	0.61	1.10	1.09	-0.1867	4.849
NBLA	-73.40202	-39.87030	13.80	3.89	3.18	0.43	0.66	0.67	-0.2013	5.483
PAGR	-73.52343	-45.16086	-0.48	4.15	14.95	0.12	0.23	0.23	-0.4334	10.022
PCGN	-72.30287	-41.53350	-3.64	1.81	4.93	0.34	0.28	0.27	0.1561	4.877
PDBL	-69.67096	-45.45724	-4.07	-0.00	0.52	0.45	0.60	0.60	-0.4774	4.973
PLNA	-71.80873	-43.62018	-6.54	1.14	-2.29	0.80	0.64	0.64	0.1195	4.841
PLRN	-72.43517	-41.99835	-10.25	6.33	-78.41	0.35	0.80	0.82	-0.5179	4.887
PLTQ	-72.69846	-46.57107	-2.95	0.83	9.70	0.51	0.40	0.39	0.0733	9.800
PMGN	-69.64240	-43.75306	-4.88	0.28	1.42	0.93	0.91	0.91	-0.0011	4.932
PMON	-72.91821	-41.46990	-1.01	3.57	2.22	0.08	0.12	0.12	-0.2040	7.910
QLLN	-73.68450	-43.14881	1.52	6.86	12.77	0.37	0.61	0.61	-0.2791	10.551
RARI	-71.34717	-35.78683	27.65	5.04	-4.37	0.41	0.25	0.23	0.2764	10.742
STMZ	-72.62987	-42.01485	-4.55	3.15	8.35	0.42	1.09	1.09	-0.4710	9.797
TPRA	-71.67515	-44.64530	-4.79	-0.45	-1.80	0.48	0.73	0.73	-0.1618	5.079
TREL	-65.37825	-43.26431	-2.47	1.33	-1.76	0.34	0.47	0.46	-0.1720	7.025
TRMS	-71.43185	-36.91761	13.59	-5.09	5.13	0.68	1.59	1.64	-0.5151	10.751
VRPL	-72.36816	-43.87057	-5.50	0.22	3.57	0.33	0.82	0.81	-0.3121	9.786
ZAPL	-70.02394	-38.82775	-0.47	-1.64	0.55	0.15	0.35	0.36	-0.5481	10.260

<sup>a</sup>GPS site velocity is expressed relative to the South America reference frame defined using GPS stations listed in Table 2. Ve, Vn, and Vu are the east, north, and up components of velocity (mm/a), respectively, with SigVe, SigVn, and SigVu being their standard errors (mm/a). CorNE is north and east correlation coefficient. Tspan is time span of measurements in years.

of the relative motion between the Nazca and South America plates [Hoffmann-Rothe *et al.*, 2006]. The southern termination of LOFZ at about 46.5–47.5°S is near the Chile triple junction where the Chile spreading ridge is being subducted. The interaction of the spreading ridge with the continental forearc has had a strong impact on the

motion of the southern LOFZ [Nelson *et al.*, 1994]. There is evidence that a predecessor of LOFZ exhibited left-lateral motion in the Mesozoic [Cembrano *et al.*, 2000].

[8] The right-lateral motion of the LOFZ appears to have accelerated in the Middle Miocene [Cembrano *et al.*, 2002]. The latest estimate of the average rate

**Table 2.** GPS Stations Defining the South America Reference Frame<sup>a</sup>

Station	Longitude	Latitude	Ve	Vn	Vu	Type	Tspan
KOUR	-52.80596	5.25218	0.54	-0.01	1.26	HV	12.296
FLIX	-80.08806	-26.29705	62.81	8.10	1.02	V	7.355
PARE	-70.91950	-53.62742	5.73	0.62	-0.29	V	6.614
PELD	-70.67493	-33.14318	20.74	6.10	0.72	V	10.509
RBSN	-78.83698	-33.62886	62.67	8.18	2.18	V	6.679
TNDL	-59.08637	-37.32423	0.97	0.29	1.25	HV	10.241
EISL	-109.38329	-27.14821	67.83	-11.20	-1.80	V	11.006
FORT	-38.42561	-3.87745	0.22	-0.25	-3.55	H	11.359
LPGS	-57.93230	-34.90675	-0.00	-0.17	1.17	HV	11.362
ESRN	-68.79857	-53.34318	1.72	2.30	1.92	V	5.660
MYMD	-69.49918	-52.15680	0.93	1.49	1.04	V	5.655
AREQ	-71.49279	-16.46551	14.07	3.83	-1.20	V	7.161
HART	27.70776	-25.88710	22.19	13.91	1.77	V	3.260
BRAZ	-47.87787	-15.94748	0.38	-0.14	-0.70	HV	10.225
PARA	-49.23095	-25.44837	-0.07	-0.19	-0.02	HV	10.008
UEPP	-51.40853	-22.11990	-0.04	0.53	0.23	HV	10.008
VICO	-42.86999	-20.76150	-0.01	-0.30	-1.32	HV	10.008
BOMJ	-43.42174	-13.25556	-1.09	0.41	-2.56	HV	10.008
CUIB	-56.06987	-15.55526	0.08	0.05	-0.64	H	10.008
IMPZ	-47.49723	-5.49177	0.25	-0.04	-1.11	HV	10.008
MANB	-60.05603	-3.11615	-0.38	-0.64	-2.73	H	8.350
UNSA	-65.40764	-24.72746	6.33	0.35	-0.31	V	10.006
CFAG	-68.23265	-31.60217	7.10	0.96	-1.59	V	9.548
TUCU	-65.23035	-26.84326	3.35	-1.10	-0.39	V	9.499
GALA	-90.30362	-0.74270	55.86	2.56	-0.22	V	6.764
ASC1	-14.41207	-7.95121	-0.38	-0.22	-2.26	H	8.990
COPO	-70.33824	-27.38453	21.36	6.54	1.05	V	8.925
LHCL	-65.59525	-38.00266	-0.31	-0.62	-1.17	HV	8.400
PMON	-72.91821	-41.46990	-1.01	3.57	2.22	V	7.910
PARC	-70.87988	-53.13696	2.13	1.71	-1.16	V	8.383
FREI	-58.98050	-62.19410	7.83	6.20	-3.39	V	7.306
PALM	-64.05112	-64.77509	10.66	0.71	1.15	V	7.691
COYQ	-71.89208	-45.51434	-4.98	-0.20	-0.07	V	7.485
PWMS	-67.58493	-54.93420	6.51	1.07	0.43	V	7.471
LKTH	-57.85074	-51.69841	-0.07	1.15	-0.19	HV	6.515
RIOP	-78.65111	-1.65060	-0.76	-10.43	1.64	V	3.120
BORC	-44.74062	-60.73978	8.69	1.18	-1.96	V	4.367

<sup>a</sup>The reference frame is realized by minimizing the horizontal H type stations that are located within the stable core of the reference plate and the vertical velocity of V type stations that are located both within the reference plate and elsewhere. Ve, Vn, and Vu are the east, north, and up components of velocity (mm/a), respectively. Tspan is time span of measurements in years.

since Pliocene is about 36 mm/a for its southern part, decreasing northward to 13 mm/a near its northern termination [Rosenau *et al.*, 2006]. The motion must have substantially slowed down from these rates, because the present margin-parallel component of the Nazca–South America motion is only about 23 mm/a according to geodetic observations [Angermann *et al.*, 1999; Kendrick *et al.*, 2003] or 28 mm/a according to the NUVEL-1a global plate motion model [DeMets *et al.*, 1994]. The most direct evidence for its modern activity is the  $M_s$  5.3 Longuimay earthquake in 1989, the  $M_w$  6.2 Hudson earthquake in 1965, and the  $M_w$  6.2 Aisen earthquake in 2007 (Figure 2). All these earthquakes are right-lateral strike-slip faulting events.

The two  $M_w$  6.2 events occurred almost in the same place. However, there have been no direct observational constraints on the LOFZ's modern rate of motion.

[9] Forearc-sliver translation accommodating the margin-parallel component of oblique convergence is a very common process at subduction zones [Fitch, 1972]. As a result of the sliver motion, the relative convergence between the sliver and the subducting plate is much less oblique, as reflected in the orientation of the slip vectors of numerous great megathrust earthquakes [e.g., Yu *et al.*, 1993; McCaffrey, 1994]. This slip partitioning translates into a type of strain partitioning: Much of the

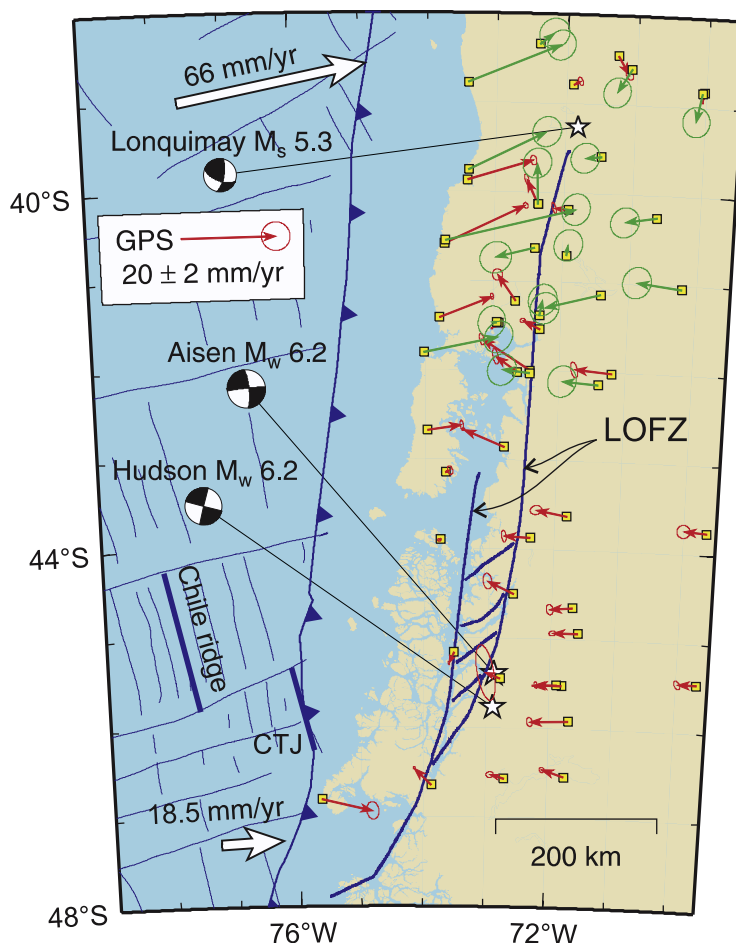


**Figure 2.** The LOFZ and GPS velocities corrected for the strike-parallel motion of the forearc sliver west of it. Labeled large arrows are plate motion vectors relative to South America. Squares indicate locations of GPS sites. New GPS data and those from *Klotz et al.* [2001] are shown with red and green arrows, respectively, with one-standard-deviation error ellipses. Stars indicate epicenters of earthquakes along the LOFZ, with their focal mechanisms shown using beach-ball diagrams (lower-hemisphere stereonet projection): the 1989  $M_s$  5.3 Lonquimay earthquake [*Barrientos and Acevedo-Aránguiz*, 1992], the 1965  $M_w$  6.2 Hudson earthquake [*Chinn and Isacks*, 1983], and the 2007  $M_w$  6.2 Aisen earthquake (U.S. Geological Survey National Earthquake Information Center: <http://neic.usgs.gov/neis/qed/>).

along-strike shear is accommodated by the permanent deformation of the upper plate along fault zones such as the LOFZ, but much of the elastic strain accumulation and release in interplate great earthquake cycles takes place in the margin-normal direction. The most recent example is the  $M_w$  9.2 great Sumatra earthquake of 2004. Although the plate convergence direction is very oblique, the coseismic slip of the Sumatra megathrust as constrained by GPS observations is much less oblique [*Chlieh et al.*, 2007]. The margin-parallel component is accommodated by the strike-slip motion of the Sumatran fault in the upper plate [*Fitch*, 1972; *McCaffrey et al.*, 2000]. In some cases, forearc motion occurs without a clearly defined strike-slip

fault system and may not be purely strike-slip. If the sliver motion has a margin-normal component, the distance between the trench and the stable part of the upper plate may change with time, such as at the central and southern Cascadia subduction zone [*Wells et al.*, 1998] and the northern Hikurangi subduction zone [*Wallace et al.*, 2004].

[10] The motion of the LOFZ is evident in our GPS measurements south of 42°S (Figure 1), although the rate of the motion cannot be accurately determined. Around 44°S, the almost 90° difference in the direction of GPS velocities across the LOFZ can only be explained by the right-lateral shear of the fault zone. No other geological models can

explain the drastic velocity rotation over such a short distance. The southward decrease in the margin-normal component of coastal GPS velocities is very likely to be caused by a southward change in the slip and locking behavior of the megathrust seismogenic zone, which will be discussed in section 4. But the change in the seismogenic zone behavior alone cannot explain why the margin-parallel velocities do not show a similar southward decrease. Considering the geological and seismological evidence for the right-lateral shear of the LOFZ, the most reasonable explanation for the sustained margin-parallel velocity is that it reflects a net northward translation of the forearc sliver west of the LOFZ.

[11] Our GPS observations shown in Figure 1 present the first geodetic evidence for the contemporary dextral motion of the LOFZ. In terms of localizing shear strain in the volcanic arc, the weakest part of the overriding plate, to accommodate the margin-parallel component of relative plate motion, the LOFZ is similar to the Sumatran fault, although the convergence obliquity at Chile is much less than at Sumatra and the LOFZ is not as long as the Sumatran fault. However, our small number of GPS stations only allows a highly simplified deformation pattern of the LOFZ to be defined. There have been no neotectonic studies that address the current deformation rate of the LOFZ, nor how the rate decreases northward.

[12] As a working hypothesis, we consider the following simple kinematical model for the LOFZ. We assume that the translation of the southern part of the forearc sliver is at a rate represented by the average strike-parallel velocity of the three GPS sites (6.5 mm/a) within the sliver between latitudes 42°S and 44°S. This rate is about three quarters of the strike-slip component of the relative motion between the Nazca and South America plates. We further assume that the rate linearly decreases northward from 42°S to the approximate northern end of the LOFZ at 39.5°S, implying a north-south shortening of the sliver over this latitudinal range. This simple model will be tested and refined by future geodetic and geological observations. The GPS velocities after this assumed sliver motion is subtracted are shown in Figure 2. The “corrected” GPS velocities west of the LOFZ are either in the opposite direction of those east of the LOFZ or negligibly small. In the following section, we use the velocity pattern of Figure 2 to constrain the model of postseismic and interseismic deformation following the 1960 earthquake. A similar approach

of removing forearc motion before modeling earthquake cycle deformation has been used by *Wang et al.* [2003].

## 4. Deformation Following the 1960 Chile Earthquake

### 4.1. Conceptual Model and Rheology

[13] As explained by *Hu et al.* [2004], the seaward motion of inland GPS sites is a consequence of stress relaxation in Earth’s viscoelastic mantle, in much the same way as postglacial rebound. Thrust motion of the subduction zone megathrust during a great interplate earthquake pulls the upper plate toward the trench. Because the instantaneous response of the Earth to sudden loading is elastic, stress is induced in the crust and upper mantle to resist deformation. Coseismic elastic deformation thus rapidly decreases with increasing distance from the rupture zone as is rather accurately described by elastic dislocation models. The longer-term response of the upper mantle is viscous, and the stress associated with the initial elastic deformation will relax. As the underlying mantle gradually loses its shear strength in this process, the stretching stress in the elastic lithosphere causes the lithosphere itself to move toward the trench. Therefore inland sites away from the rupture that were unable to have significant coseismic motion can slowly catch up after the earthquake, manifesting as seaward motion in GPS measurements. At the same time, coastal sites have begun to move landward as a result of the relocking of the megathrust, to accumulate strain energy for the next great earthquake. After a long time of locking, the inland sites will eventually stop their seaward motion and move landward [*Wang et al.*, 2001].

[14] Postseismic seaward motion of distal inland sites has also been observed in the region affected by the  $M_w$  9.2 Alaska earthquake of 1964 [*Savage et al.*, 1999; *Frey Mueller et al.*, 2000]. It is currently taking place at a fast rate in the region affected by the 2004 great Sumatra earthquake [e.g., *Pollitz et al.*, 2006; *Chlieh et al.*, 2007; *Paul et al.*, 2007], although the rate is expected to decrease substantially in the next couple of decades as can be inferred from the Chile model of *Hu et al.* [2004]. *Hu et al.* [2004] have shown that the duration of the seaward motion depends on the along-strike length of the rupture. Rupture lengths of most interplate earthquakes are less than a couple of hundred kilometers, and the seaward

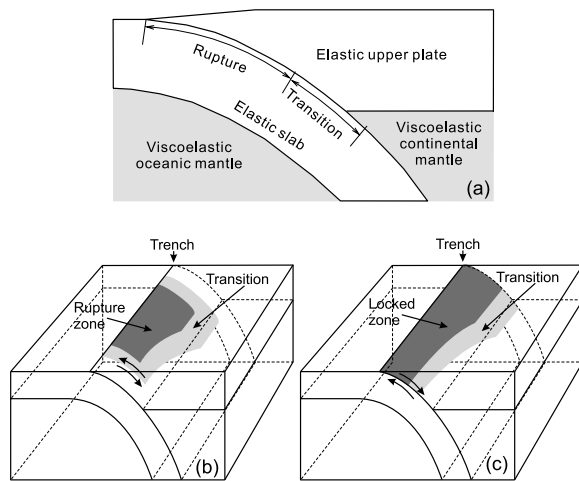


**Figure 3.** (a) Schematic illustration of the fault model of this work. (b) Coseismic slip model. (c) Backslip model for fault locking after the earthquake. Slip in Figure 3b or backslip rate in Figure 3c tapers to zero over the transition zone (lighter shading). The model is modified from the model of uniform seismogenic zone width of *Hu et al.* [2004].

motion of inland sites quickly slows down before eventually reversing direction, as is observed in both the CAP and SAGA GPS networks in the region of the 1995,  $M_w = 8$ , Antofagasta earthquake [e.g., *Klotz*, 2006].

[15] The viscoelastic mantle rheology mentioned above is of the Maxwell type, and the viscous component of the deformation is usually assumed to be Newtonian. The time for the mode of deformation to change from predominantly elastic to predominantly viscous is referred to as the Maxwell time ( $T_M$ ). With the continental upper mantle viscosity values of around  $10^{19}$  Pa s commonly used in subduction zone postseismic stress relaxation models [*Wang*, 2007],  $T_M$  is of the order of a decade. The rate of stress relaxation of a system consisting units of different mechanical properties depends on the exact configuration of the system. For the simple subduction zone model employed by *Hu et al.* [2004] and in this work (Figure 3), which has two elastic plates and viscoelastic continental and oceanic mantle, the system is fully relaxed in about  $20 T_M$  of the continental mantle.

[16] Modern geodetic observations have shown that the linear Maxwell viscoelastic rheology, widely used in postglacial and postseismic deformation modeling, is inadequate for modeling short-term postseismic deformation. The rate of the

velocity change (deceleration of the site) within a few years of an earthquake observed at continuous GPS stations is much too fast to be explained using the linear Maxwell viscoelasticity. The mechanism of the short-term deformation is still a matter of conjecture, however. Models of short-term post-seismic deformation include afterslip of the fault area around the rupture zone [*Melbourne et al.*, 2002], transient rheology [*Pollitz et al.*, 2006], and nonlinear (power law) rheology [*Freed et al.*, 2006]. Afterslip and transient rheology are unavoidable on the basis of rupture mechanics and rock physics, but the parameters involved are practically unconstrained at present. Power law parameters are well determined in laboratories under the condition of steady state deformation (constant stress and strain rate), but it is highly debatable to what degree the steady state rheology is applicable to the transient short-term deformation.

[17] Regardless of the mechanisms of the short-term deformation, the rate of the velocity change becomes very small a decade or more after the earthquake, such that the linear Maxwell viscoelasticity is a very reasonable approximation for decadal and century-scale deformation models [*Wang*, 2007]. For our purpose of modeling the deformation a few decades after the 1960 earthquake, it suffices to “lump” the rapid short-term deformation into the coseismic deformation. For this purpose, we need to use a rather wide coseismic rupture zone and a wide zone of downdip transition over which the slip tapers to zero (Figure 3).

#### 4.2. Numerical Model

[18] Our numerical model is a modification of the three-dimensional (3-D) finite element model of *Hu et al.* [2004]. The model is developed in a Cartesian coordinate system. The results on the flat surface ( $x$ - $y$  plane) of the Cartesian model mesh are mapped onto the ellipsoidal surface of the Earth via Lambert Conformal map projection for comparison with GPS observations. Free parameters are determined by trial and error through visual assessment of the fit to GPS data.

[19] The following aspects of the new model are identical to the model of *Hu et al.* [2004]. We use the GPS-determined Nazca–South America convergence rate of 66 mm/a [*Angermann et al.*, 1999], which is similar to the rate reported by *Kendrick et al.* [2003], rather than the NUVEL-1a long-term tectonic rate of 80 mm/a [*DeMets et al.*, 1994]. The viscosities of the continental mantle and oceanic mantle are assumed to be  $2.5 \times 10^{19}$  Pa s

and  $10^{20}$  Pa s, respectively. The higher viscosity value for the oceanic mantle yields a more reasonable vertical deformation pattern following a model earthquake, while the horizontal deformation pattern is very insensitive to this parameter [Hu *et al.*, 2004]. The elastic upper and lower plates are assumed to be 40 km and 30 km thick, respectively, both with a Young's modulus of 120 GPa. The mantle is assumed to have a Young's modulus of 160 GPa. The Poisson's ratio and density are uniformly 0.25 and  $3300 \text{ kg/m}^3$ , respectively. The effect of gravity on deformation is simulated using a prestress advection approach commonly employed in postglacial rebound modeling [Peltier, 1974]. Numerically, the effect is incorporated as a restoring body force proportional to density and vertical displacement that tends to bring a perturbed system back to a hydrostatic state [Wang *et al.*, 2001]. Faulting is modeled using a 3-D version of the split-node method [Melosh and Raefsky, 1981]. The effect of fault locking is simulated using the standard back-slip recipe, assuming processes unrelated to great earthquake cycles have been subtracted [Savage, 1983; Wang, 2007]. Downdip of the uniform coseismic slip (or interseismic back-slip) zone, there is a transition zone over which the slip (or back slip) linearly tapers to zero (Figure 3). The width of the transition zone is fixed at  $2/3$  that of the zone of uniform slip (or back slip). Hu *et al.* [2004] provided justifications for the choice of parameter values and conducted numerous tests on the sensitivity of model results to the parameters.

[20] The following aspects of the new model are different from the model of Hu *et al.* [2004]. Instead of a uniform convergence rate of 66 mm/a, we use a rate of 18.5 mm/a south of the Chile triple junction to represent the much slower convergence between the Antarctica plate and South America plate (Figure 1). This rate is obtained using an Antarctica–South America Euler vector derived by one of the authors of this paper (R.S.). It is similar to those obtained using other GPS-constrained Antarctica–South America Euler vectors reported in the literature [Sella *et al.*, 2002; Prawirodirdjo and Bock, 2004] and is slightly smaller than the NUVEL-1a value of 20 mm/a. Compared to the model of Hu *et al.* [2004], the assumed 1960 rupture extends slightly further south in order to give a better fit to the GPS data in that area, but the extension is well within uncertainties in the geological and seismological constraints on the southern termination of the rupture. Another small difference from the model of Hu *et al.* [2004] is

that we have made the locked zone north of the 1960 rupture wider to improve the fit to the GPS data. These modifications to the model of Hu *et al.* [2004] are straightforward operations. The main new challenge is to account for the southward decrease in the speed of landward motion of coastal GPS sites (Figure 2). To explain the southward decrease, various options are available.

[21] For example, we may assume a southward narrowing of the megathrust seismogenic zone. A narrower rupture zone in 1960 and a narrower locked zone afterward can reduce the landward velocities of the coastal sites. This option is consistent with the hypothesis that the downdip width of the seismogenic zone is thermally controlled. As we move south along the margin, the age of the incoming plate gradually decreases to zero at the Chile triple junction, accompanied with an increase in heat flow [Cande *et al.*, 1987]. The southern termination of the 1960 rupture is very likely to be related to the high temperature near the Chile triple junction. For margins with very young incoming plates, the downdip limit of the seismogenic zone is expected to be controlled by a temperature of about  $350^\circ\text{C}$  [Hyndman and Wang, 1993]. Although detailed thermal models are not yet available, there is no doubt that the temperature along a given megathrust depth contour increases southward, and therefore the thermally controlled downdip limit of the seismogenic zone becomes shallower.

[22] Another option is to assume no southward change in the seismogenic zone but attribute the southward decrease of coastal velocities entirely to the sliver motion discussed in section 3. This would require the motion of the southern part of the sliver to have a westward component in addition to the northward component. The northward component has been removed from velocities shown in Figure 1 to obtain velocities shown in Figure 2. If an additional westward component were also removed, velocities in the southern part of the sliver could become similar to those to the north. We do not pursue this option, because it would require the LOFZ to have an opening rate of a few mm/a, which contradicts the current recognition of the LOFZ as a transcurrent or transpressive system.

### 4.3. Model Results

[23] In Figure 4, we show the results of a model with a southward narrowing of both the 1960 rupture zone and the subsequent locked zone.

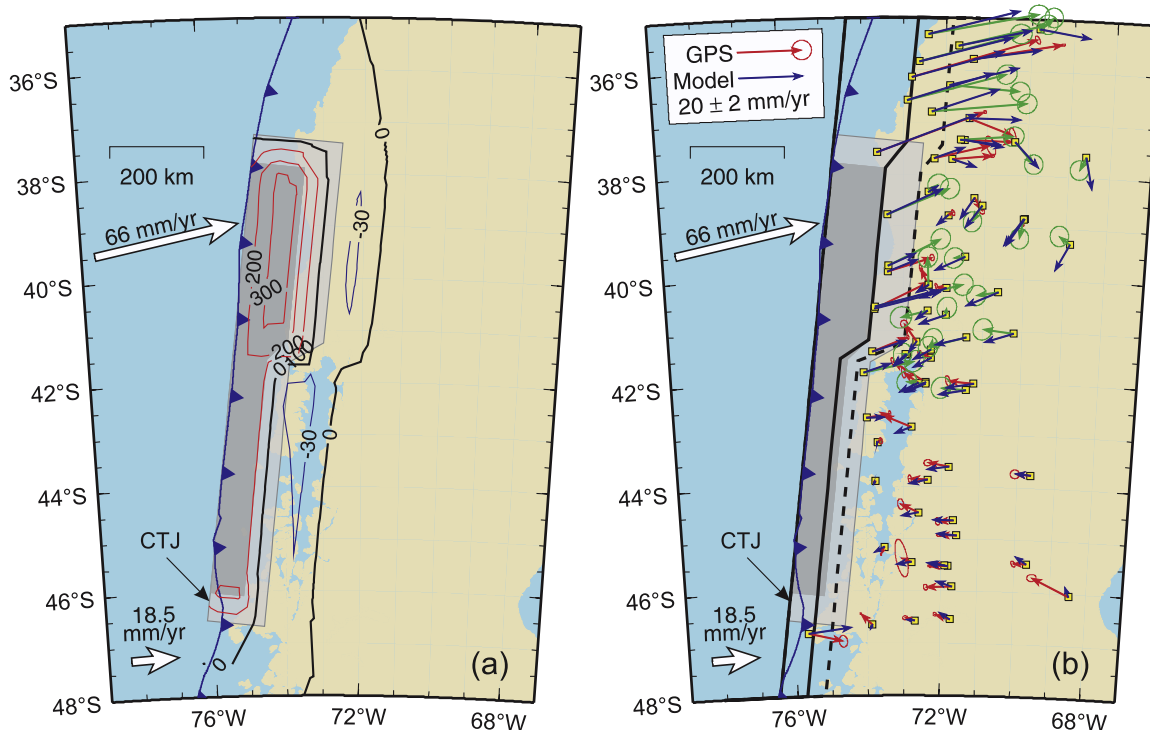


**Figure 4.** Results for a model with southward narrowing of both the 1960 rupture zone and subsequent locked zone. (a) Coseismic vertical deformation. Contours are in centimeters. For the subsidence area, only the  $-30$  cm contour is shown. (b) Comparison of model velocities calculated 40 a after the earthquake (blue arrows) with sliver-motion-corrected GPS observations. Squares indicate locations of GPS sites. GPS velocities from this work and *Klotz et al.* [2001] are shown with red and green arrows, respectively, with one-standard-deviation error ellipses. In both Figure 4a and Figure 4b, dark shading and light shading represent the rupture (20 m slip) and coseismic transition zones, respectively. In Figure 4b, thick solid and dashed lines outline the locked and interseismic transition zones, respectively.

The reasoning for assuming the southward narrowing has been discussed in section 4.2. In this model, we assume a uniform coseismic slip of 20 m along strike in the rupture zone and complete locking of the locked zone afterward, as done by *Hu et al.* [2004]. This rupture scenario gives an  $M_w$  of 9.52, similar to the seismologically determined  $M_w$  of 9.5 for the 1960 event [*Kanamori, 1977*].

[24] We allow the southward narrowing to occur in a stepwise fashion (Figure 4), consistent with the along-strike stepwise change in the age of the incoming plate as indicated by offshore magnetic anomalies (Figure 1). The age of the oceanic plate jumps across transform faults (and their landward extension beneath the forearc) that are oriented at a large angle with the Chile trench. For example, major changes in age occur around 37–38°S and 41–42°S (Figure 1). Between two adjacent transform faults, the age of the plate is nearly constant. Without detailed 3-D thermal modeling, the along-strike change in the thermal regime as a conse-

quence of the stepwise age change cannot be quantified. Even if the temperatures were precisely known, there still is large uncertainty whether the downdip limit of the seismogenic zone exactly follows an isotherm. The widths of the rupture/locked and transition zones for the northern half of the 1960 earthquake zone are 120 km and 80 km, the same as used by *Hu et al.* [2004]. The widths of the southern half are chosen to fit the GPS velocities.

[25] After numerous numerical tests, we conclude that if the width of the 1960 rupture zone and the width of the subsequent locked zone are the same, this model cannot simultaneously fit the GPS observations in both the coastal and inland areas south of 42°S. Depending on the width, the model would predict either coastal velocities that are too large or inland velocities that are too small. With the locked zone assumed to be slightly wider than the rupture zone, the model can fit the general pattern of the GPS observations reasonably well (Figure 4b). The southward narrowing of both the

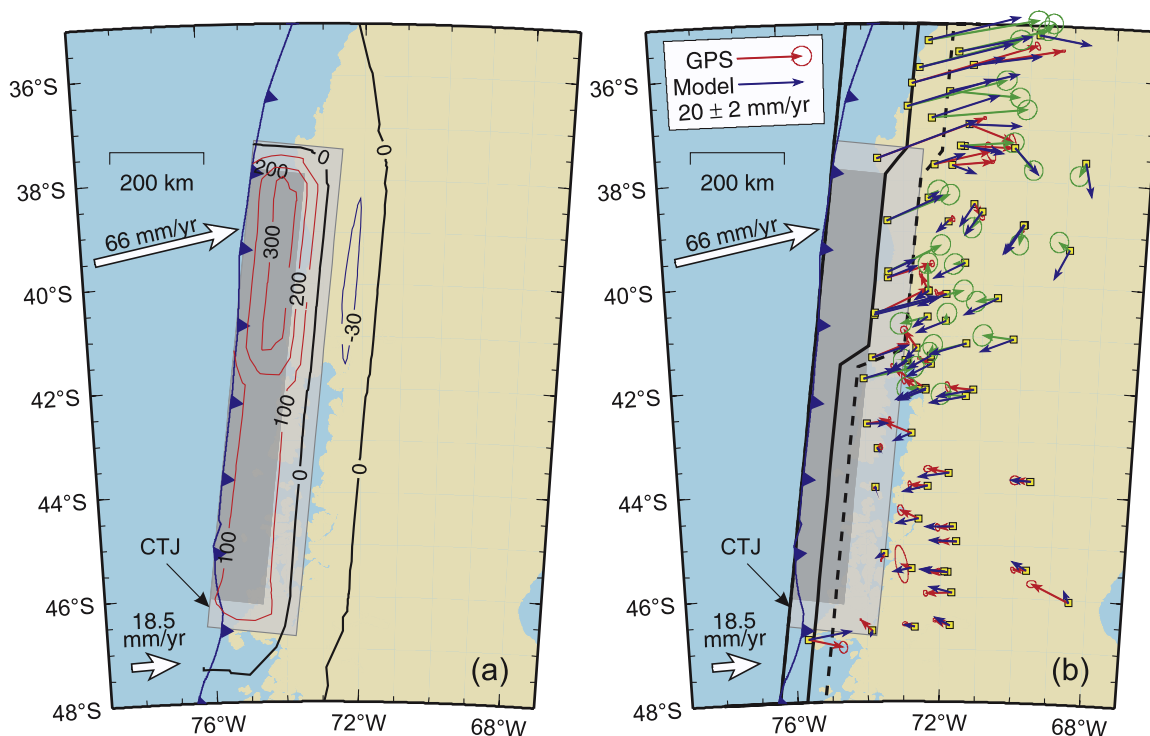


**Figure 5.** Results for a model with a uniform width of the 1960 rupture zone but southward narrowing of the locked zone. (a) Coseismic vertical deformation. Contours are in centimeters. For the subsidence area, only the  $-30$  cm contour is shown. (b) Comparison of model velocities calculated 40 a after the earthquake (blue arrows) with sliver-motion-corrected GPS observations. Squares indicate locations of GPS sites. GPS velocities from this work and *Klotz et al.* [2001] are shown with red and green arrows, respectively, with one-standard-deviation error ellipses. In both Figure 5a and Figure 5b, dark shading and light shading represent the rupture (20 m slip in the northern half and 10 m in the southern half) and coseismic transition zones, respectively. In Figure 5b, thick solid and dashed lines outline the locked and interseismic transition zones, respectively.

1960 rupture zone and the subsequent locked zone causes the crustal deformation pattern to be “shifted” toward the trench in the south. Near the trench and directly above the locked zone, the landward motion is still at the plate convergence velocity, but the velocity decreases rapidly landward and becomes zero just west of the LOFZ.

[26] The difficulty with assuming a nonuniform width of the 1960 rupture is that it cannot produce a coseismic vertical deformation pattern as uniform as that observed by Plafker in 1968 [Plafker and Savage, 1970]. His deformation pattern, particularly the “hinge line” between uplift and subsidence, would suggest a fairly uniform rupture width [Barrientos and Ward, 1990]. The pattern shown in Figure 4a in the northern half of the 1960 rupture zone is the same as that of *Hu et al.* [2004]. Here the hinge line is located more landward than Plafker’s, because of the wide rupture zone used to account for the effects of continuing short-term postseismic deformation after 1968, as discussed in

section 4.1 and *Hu et al.* [2004]. In the southern part where the seismogenic zone is assumed to be narrower, the hinge line is more consistent with that of Plafker’s. If the pattern in Figure 4a is correct, it implies that the rapid short-term postseismic deformation in the south had been largely diminished when Plafker visited these sites in 1968, such that we do not need to use a wider-than-actual rupture zone for this part of the model. Conceivably, the warmer thermal regime in the south may give rise to a faster process of short-term deformation by affecting frictional properties of the megathrust and rock rheology of the shallow part of the subduction zone.

[27] If we keep the width of the 1960 rupture zone uniform along strike, we can still satisfy the GPS observations by making the coseismic slip smaller in the southern half. In the model shown in Figure 5, coseismic slip in the southern half of the uniform-width rupture zone is 10 m, 50% of the value in the north. The change from 20 m to 10 m

slip is assumed to occur in the same place as the width change in the model shown in Figure 4. The moment magnitude for this rupture scenario is 9.49. Fault locking after the earthquake is identical to that of the model shown in Figure 4. A comparison of Figure 5b with Figure 4b shows that, in affecting horizontal deformation, making the coseismic slip smaller is similar to making the rupture zone narrower. The vertical deformation pattern produced by the model of uniform rupture width is more comparable with Plafker's observed pattern, except for the more landward location of the hinge line for reasons explained above.

[28] No single model can uniquely explain the GPS observations shown in Figures 1 and 2. For a site sufficiently away from the trench, a narrower rupture zone with a larger coseismic slip or a wider rupture zone with a smaller slip can have a similar effect, a narrower locked zone with complete locking or a wider locked zone with incomplete locking can have a similar effect, and so forth. With careful matching of parameters, a model involving incomplete interseismic locking can also fit the GPS observations. A southward decrease in the thickness of the Nazca plate in the model, also compatible with its younger age in the south, can also to some degree account for the southward decrease in coastal margin-normal velocities. Given the many simplifying assumptions required to set up the numerical model, we do not think selecting the best parameter combination on the basis of a statistical measure of data fit is very meaningful. The two models shown in Figures 4 and 5 serve to demonstrate that the southward decrease in margin-normal velocities of near-coast GPS sites can be adequately explained by a southward change in the width or frictional properties of the seismogenic zone.

## 5. Conclusions

[29] 1. GPS velocities determined by campaign surveys conducted during 1993–2005 have confirmed the presence of opposing motion of coastal and inland sites previously reported by *Klotz et al.* [2001] for the northern part of the region affected by the  $M_w$  9.5 great Chile earthquake of 1960. The new observations show that the opposing motion is present also in the southern part and throughout the 1960 earthquake zone. The observations thus support the concept of prolonged postseismic deformation after an earthquake of very large

along-strike length. The landward motion of coastal sites reflects the current locking of the plate interface, and the seaward motion of inland sites indicates viscoelastic relaxation of the stress induced by the 1960 earthquake.

[30] 2. The new GPS observations provide the first geodetic evidence for the active dextral shear motion of the LOFZ and the consequent northward translation of a forearc sliver. The observed motion of the forearc can be described as block translation at 6.5 mm/a, with the rate tapering to zero northward at the northern termination of the LOFZ. Our finding is consistent with the model of forearc sliver motion accommodating the strike-slip component of oblique plate convergence. It suggests the need for further geological and geodetic investigation of the modern motion of the LOFZ.

[31] 3. The new GPS observations indicate a southward decrease in the current margin-normal motion of the coastal area in the region of the 1960 rupture. The present data do not allow a unique and unambiguous explanation for this change. Our preferred explanation is that the southward decrease in the age of the subducting plate and consequently the increase in the temperature on the plate interface give rise to changes in the width or frictional properties of the megathrust seismogenic zone. The southern part of the presently locked portion of the plate interface is likely to be narrower. A modification of an earlier 3-D viscoelastic postseismic deformation model of *Hu et al.* [2004] to account for this southward change can explain the first-order pattern of the GPS observations.

## Acknowledgments

[32] We thank the Instituto Geografico Militar de Chile, UNAVCO, Gino Cassassa and the Universidad de Magallanes, Romualdo Moreno Arias, Alvaro Giannini, and Sabine Comes for their assistance with the GPS measurements in Chile, and Adolfo Garcia and Horacio Barrera of Instituto Geografico Militar Argentina for their assistance with the GPS measurements in Argentina. We would also like to acknowledge the encouragement and the assistance of Detleff Angermann and Jurgen Klotz of CAP's sister project, SAGA; the GPS campaign in 1994 was a collaborative effort between CAP and SAGA. J. He wrote the computer program, PGCvisel, that we used to develop the 3-D finite element model in this work and provided assistance in the modeling work. We thank R. Bürgmann and H. Dragert for their valuable comments. This is Geological Survey of Canada contribution 20070241 and the Center for Earthquake Research and Information (U. Memphis) contribution 514.

## References

- Angermann, D., J. Klotz, and C. Reigber (1999), Space-geodetic estimation of the Nazca-South America Euler vector, *Earth Planet. Sci. Lett.*, *171*, 329–334.
- Barrientos, S. E., and P. S. Acevedo-Aranguiz (1992), Seismological aspects of the 1988–1989 Lonquimay (Chile) volcanic eruption, *J. Volcanol. Geotherm. Res.*, *53*, 73–87.
- Barrientos, S. E., and S. N. Ward (1990), The 1960 Chile earthquake: Inversion for slip distribution from surface deformation, *Geophys. J. Int.*, *103*, 589–598.
- Brooks, B. A., M. Bevis, R. Smalley, Jr., E. Kendrick, R. Manceda, E. Lauria, R. Maturana, and M. Araujo (2003), Crustal motion in the Southern Andes (26°–36°S): Do the Andes behave like a microplate?, *Geochem. Geophys. Geosyst.*, *4*(10), 1085, doi:10.1029/2003GC000505.
- Cande, S. C., R. B. Leslie, J. C. Parra, and M. Hobart (1987), Interaction between the Chile ridge and Chile trench: Geophysical and geothermal evidence, *J. Geophys. Res.*, *92*, 495–520.
- Cembrano, J., E. Schermer, A. Sanhueza, and A. Lavenu (2000), Along strike variations in the nature and timing of deformation along the intra-arc shear zone, the Liquine Ofqui fault zone, southern Chilean Andes, *Tectonophysics*, *319*, 129–149.
- Cembrano, J., A. Lavenu, P. Reynolds, G. Arancibia, G. Lopez, and A. Sanhueza (2002), Late Cenozoic transpressional ductile deformation north of the Nazca–South America–Antarctica triple junction, *Tectonophysics*, *354*, 289–314.
- Chinn, D. S., and B. L. Isacks (1983), Accurate source depths and focal mechanisms of shallow earthquakes in western South America and in the New Hebrides island arc, *Tectonics*, *2*(6), 529–563.
- Chlieh, M., J.-P. Avouac, V. Hjorleifsdottir, T.-R. A. Song, C. Ji, K. Sieh, A. Sladen, H. Hebert, L. Prawirodirdjo, Y. Bock, and J. Galetzka (2007), Coseismic slip and afterslip of the great Mw 9.15 Sumatra-Andaman earthquake of 2004, *Bull. Seismol. Soc. Am.*, *97*(1A), S152–S173.
- Cifuentes, I. L. (1989), The 1960 Chilean Earthquakes, *J. Geophys. Res.*, *94*, 665–680.
- DeMets, C., R. G. Gordon, D. F. Argus, and S. Stein (1994), Effect of recent revisions to the geomagnetic reversal time scale on estimates of current plate motions, *Geophys. Res. Lett.*, *21*(20), 2191–2194.
- Fitch, T. J. (1972), Plate convergence, transcurrent faults and internal deformation adjacent to southeast Asia and the western Pacific, *J. Geophys. Res.*, *77*, 4432–4460.
- Freed, A. M., R. Bürgmann, E. Calais, and J. Freymueller (2006), Stress-dependent power-law flow in the upper mantle following the 2002 Denali, Alaska, earthquake, *Earth Planet. Sci. Lett.*, *252*, 481–489.
- Freymueller, J. T., S. C. Cohen, and H. J. Fletcher (2000), Spatial variations in continuously monitoring GPS stations about 100 to 250 km from present-day deformation, Kenai Peninsula, Alaska, and their implications, *J. Geophys. Res.*, *105*, 8079–8101.
- Hoffmann-Rothe, A., N. Kukowski, G. Dresen, H. Echter, O. Oncken, J. Klotz, E. Scheuber, and A. Kellner (2006), Oblique convergence along the Chilean margin: Partitioning, margin-parallel faulting and force interaction at the plate interface, in *The Andes: Active Subduction Orogeny*, edited by O. Oncken et al., pp. 125–146, Springer, Berlin.
- Hu, Y., K. Wang, J. He, J. Klotz, and G. Khazaradze (2004), Three-dimensional viscoelastic finite element model for postseismic deformation of the great 1960 Chile earthquake, *J. Geophys. Res.*, *109*, B12403, doi:10.1029/2004JB003163.
- Hyndman, R. D., and K. Wang (1993), Thermal constraints on the zone of major thrust earthquake failure: The Cascadia subduction zone, *J. Geophys. Res.*, *98*, 2039–2060.
- Kanamori, H. (1977), The energy release in great earthquake, *J. Geophys. Res.*, *82*, 2981–2987.
- Kendrick, E., M. Bevis, R. Smalley, R. Barriga, R. Maturana, F. Galbán, F. Forconesi, V. H. Ríos, and J. Normandeau (1997), Preliminary results of the Central Andes GPS Project, *Eos Trans. AGU*, *78*(46), Fall Meet. Suppl., F167.
- Kendrick, E., M. Bevis, R. Smalley, Jr., and B. Brooks (2001), An integrated crustal velocity field for the central Andes, *Geochem. Geophys. Geosyst.*, *2*(11), doi:10.1029/2001GC000191.
- Kendrick, E., M. Bevis, R. Smalley, Jr., B. Brooks, R. B. Vargas, E. Lauria, and L. P. S. Fortes (2003), The Nazca–South America Euler vector and its rate of change, *J. S. Am. Earth Sci.*, *16*, 125–131.
- Khazaradze, G., K. Wang, J. Klotz, Y. Hu, and J. He (2002), Prolonged post-seismic deformation of the 1960 great Chile earthquake and implications for mantle rheology, *Geophys. Res. Lett.*, *29*(22), 2050, doi:10.1029/2002GL015986.
- Klotz, J. (2006), Long-term signals in the present-day deformation field of the central and southern Andes and constraints on the viscosity of the Earth's upper mantle, in *The Andes: Active subduction Orogeny*, edited by O. Oncken et al., pp. 65–89, Springer, Berlin.
- Klotz, J., G. Khazaradze, D. Angermann, C. Reigber, R. Perdomo, and O. Cifuentes (2001), Earthquake cycle dominates contemporary crustal deformation in Central and Southern Andes, *Earth Planet. Sci. Lett.*, *193*, 437–446.
- McCaffrey, R. (1994), Global variability in subduction thrust zone—Forearc systems *Pure Appl. Geophys.*, *142*(1), 173–224.
- McCaffrey, R., P. Zwick, Y. Bock, L. Prawirodirdjo, J. Genrich, C. Stevens, S. Puntodewo, and C. Subarya (2000), Strain partitioning during oblique plate convergence in northern Sumatra: Geodetic observations and numerical modeling, *J. Geophys. Res.*, *105*, 28,363–28,375.
- Melbourne, T. I., F. H. Webb, J. M. Stock, and C. Reigber (2002), Rapid postseismic transients in subduction zones from continuous GPS, *J. Geophys. Res.*, *107*(B10), 2241, doi:10.1029/2001JB000555.
- Melosh, H. J., and A. Raefsky (1981), A simple and efficient method for introducing faults into finite element computations, *Bull. Seismol. Soc. Am.*, *71*, 1391–1400.
- Nelson, E., R. Forsythe, and I. Arit (1994), Ridge collision tectonics in terrane development, *J. S. Am. Earth Sci.*, *7*, 271–278.
- Paul, J., A. R. Lowry, R. Bilham, S. Sen, and R. Smalley, Jr. (2007), Postseismic deformation of the Andaman Islands following the 26 December 2004 Great Sumatra-Andaman earthquake, *Geophys. Res. Lett.*, doi:10.1029/2007GL031024, in press.
- Peltier, W. R. (1974), The impulse response of a Maxwell Earth, *Rev. Geophys.*, *12*, 649–668.
- Plafker, G. (1972), Alaskan earthquake of 1964 and Chilean earthquake of 1960: Implications for arc tectonics, *J. Geophys. Res.*, *77*, 901–925.
- Plafker, G., and J. C. Savage (1970), Mechanism of the Chilean earthquake of May 21 and 22, 1960, *Geol. Soc. Am. Bull.*, *81*, 1001–1030.
- Pollitz, F. F., R. Bürgmann, and P. Banerjee (2006), Post-seismic relaxation following the great 2004 Sumatra-Andaman earth-

- quake on a compressible self-gravitating Earth, *Geophys. J. Int.*, *167*, 397–420.
- Prawirodirdjo, L., and Y. Bock (2004), Instantaneous global plate motion model from 12 years of continuous GPS observations, *J. Geophys. Res.*, *109*, B08405, doi:10.1029/2003JB002944.
- Rosenau, M., D. Melnick, and H. Echtler (2006), Kinematic constraints on intra-arc shear and strain partitioning in the southern Andes between 38°S and 42°S latitude, *Tectonics*, *25*, TC4013, doi:10.1029/2005TC001943.
- Savage, J. C. (1983), A dislocation model of strain accumulation and release at a subduction zone, *J. Geophys. Res.*, *88*, 4984–4996.
- Savage, J. C., J. L. Svarc, and W. H. Prescott (1999), Deformation across the Alaska-Aleutian subduction zone near Kodiak, *Geophys. Res. Lett.*, *26*, 2117–2120.
- Sella, G. F., T. H. Dixon, and A. Mao (2002), REVEL: A model for Recent plate velocities from space geodesy, *J. Geophys. Res.*, *107*(B4), 2081, doi:10.1029/2000JB000033.
- Wallace, L. M., J. Beavan, R. McCaffrey, and D. Darby (2004), Subduction zone coupling and tectonic block rotations in the North Island, New Zealand, *J. Geophys. Res.*, *109*, B12406, doi:10.1029/2004JB003241.
- Wang, K. (2007), Elastic and viscoelastic models of subduction earthquake cycles, in *The Seismogenic Zone of Subduction Thrust Faults*, edited by T. H. Dixon and J. C. Moore, pp. 540–575, Columbia Univ. Press, New York.
- Wang, K., J. He, H. Dragert, and T. James (2001), Three-dimensional viscoelastic interseismic deformation model for the Cascadia subduction zone, *Earth Planets Space*, *53*, 295–306.
- Wang, K., R. Wells, S. Mazzotti, R. D. Hyndman, and T. Sagiya (2003), A revised dislocation model of interseismic deformation of the Cascadia subduction zone, *J. Geophys. Res.*, *108*(B1), 2026, doi:10.1029/2001JB001227.
- Wells, R. E., C. S. Weaver, and R. J. Blakely (1998), Forearc migration in Cascadia and its neotectonic significance, *Geology*, *26*, 759–762.
- Yu, G., S. Wesnousky, and G. Ekström (1993), Slip partitioning along major convergence plate boundaries, *Pure Appl. Geophys.*, *140*(2), 183–210.